JOURNAL OF SPACECRAFT AND ROCKETS
Vol. 41, No. 2, March–April 2004

Numerical Simulation of a Spinning Missile with Dithering Canards Using Unstructured Grids

Eric L. Blades* and David L. Marcum†
Mississippi State University, Mississippi State, Mississippi 39762-9627

Euler and Navier–Stokes solutions were obtained using an unstructured-grid approach to predict the aerodynamic performance of a spinning missile with dithering canards. Integrated force and moment coefficients were computed, along with helicity contours to track the horseshoe vortices generated by the canards. Comparisons were made to determine the effect of grid resolution and viscous effects. The grid-resolution study was performed using three levels of refinement. Comparison of the viscous and inviscid force and moment coefficients revealed that the viscous effects were not significant for this low angle of attack. The largest viscous contribution was to the axial force, which was approximately 10% of the total axial force. Overall the viscous effects were minimal because the flow is supersonic and remains attached and there are no regions of separated flow where viscous effects are important. The vortices are due to the pressure differences acting on the canards and not due to viscous boundary-layer separation along the missile body. It was found that, at certain roll orientations, the canards do impinge on the tail fins. Solution comparisons were made to results from another high-resolution viscous flow solver and to experimental data and the results compared favorably to both.

Nomenclature

a	=	speed of sound
a_t	=	control volume grid speed
C_A	=	axial force coefficient
C_l	=	rolling moment coefficient
C_m	=	pitching moment coefficient
C_N	=	normal force coefficient
C_n	=	yawing moment coefficient
C_Y	=	side force coefficient
E	=	total energy per unit volume
$\boldsymbol{F}$	=	inviscid flux vector
$\boldsymbol{G}$	=	viscous flux vector
H	=	total enthalpy per unit volume, helicity
L	=	reference length
M	=	Mach number
$\hat{\boldsymbol{n}}$	=	control volume unit normal vector
P	=	static pressure
$\boldsymbol{Q}$	=	vector of dependent variables
R	=	ideal gas constant
Re	=	Reynolds number
S	=	reference area
T	=	temperature
U	=	velocity magnitude
$\boldsymbol{V}$	=	velocity vector
α	=	angle of attack
Θ	=	velocity normal to control volume face
θ	=	roll angle
μ	=	fluid molecular viscosity
μ_t	=	turbulent eddy viscosity
ρ	=	fluid density
ρu, ρv, ρw	=	Cartesian momentum components
τ	=	viscous stress tensor
Ω	=	roll rate, Hz; control volume
$\boldsymbol{\omega}$	=	vorticity vector

Subscripts

∞	=	freestream value
x, y, z	=	Cartesian component directions

Received 13 June 2002; revision received 7 May 2003; accepted for publication 13 May 2003. Copyright © 2003 by Eric L. Blades and David L. Marcum. Published by the American Institute of Aeronautics and Astronautics, Inc., with permission. Copies of this paper may be made for personal or internal use, on condition that the copier pay the $10.00 per-copy fee to the Copyright Clearance Center, Inc., 222 Rosewood Drive, Danvers, MA 01923; include the code 0022-4650/04 $10.00 in correspondence with the CCC.

*Research Associate, Computational Simulation and Design Center, Engineering Research Center, Department of Mechanical Engineering. Member AIAA.

†Director, Computational Simulation and Design Center, Engineering Research Center, Department of Mechanical Engineering. Senior Member AIAA.

Introduction

THE advancement of computational fluid dynamics (CFD) has greatly influenced the design and development of projectiles and missiles. Advances in computer technology and state-of-the-art numerical procedures have enabled time-accurate, high-resolution solutions for very large, complex stationary geometries in a relatively modest amount of time. The ability to perform simulations for dynamic geometries that involve the relative motion between the missile and the control surfaces is a significant challenge for even the most state-of-the-art computational approaches and is a computationally intensive problem. The goal of this work is to demonstrate an unstructured-grid approach for the high-fidelity aerodynamic simulations of a spinning missile with moveable control surfaces. Other grid topology approaches have been successfully applied to this same problem: Murman et al.[1] applied a Cartesian method and Hall[2] and Nygaard et al.[3] used Chimera overset structured-grid methods.

The aerodynamic performance of a spinning missile with dithering control surfaces was investigated. Both Euler and Navier–Stokes solutions were obtained for the spinning missile using the unstructured unsteady computation of field equations (U^2NCLE) flow solver. For the aerodynamic conditions considered in this work, the required resolution for accurate prediction of the aerodynamic forces acting on the body is investigated as are the relative importance of the viscous effects and different canard dither patterns. In addition, it was of interest to track the vortices generated by the moving canards to determine whether they ultimately impinge on the tail fins and to examine their impact on the forces and moments, which influence the aerodynamic performance of the missile.

Geometry and Unstructured Mesh

The missile configuration used in the numerical simulations is shown in Fig. 1. The missile has a hemispherical nose, cylindrical fuselage, a boattail section, two moveable canards, and four stationary tail fins. The fuselage has a fineness ratio (length to diameter) of approximately 20. The four tail fins are located at 90-deg increments circumferentially around the tail section. The tail fins are designed to

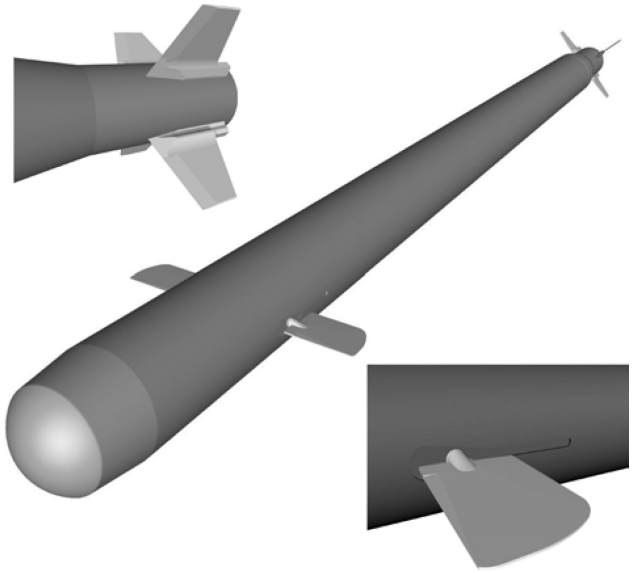

Fig. 1 Missile geometry.

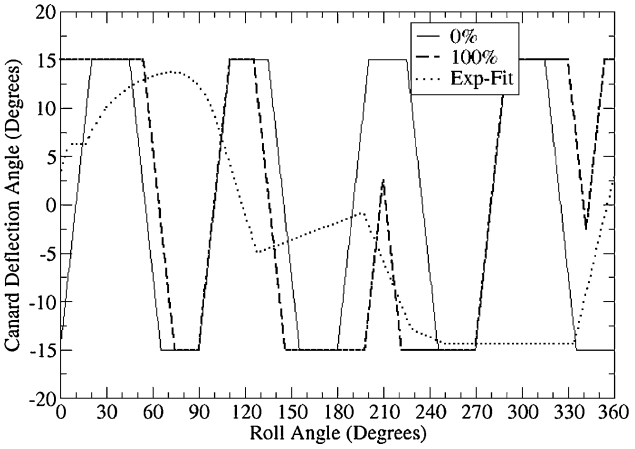

Fig. 2 Canard command levels.

induce the entire missile to spin about its longitudinal axis and they are canted 1 deg to generate a left-handed roll. Yaw and pitch control is actuated using the two interconnected canards. The canards can rotate ±15 deg from their zero-deflection position shown in Fig. 1. As the missile spins, the canards change pitch position to perform vehicle maneuvers. The motion of the canards is synchronous and specified by a canard command schedule. For the present work, two different schedules (0 and 100% command level) were used and are shown in Fig. 2 for a missile spin rate of 8.75 Hz. The time required for the canards to move between the maximum and minimum deflection angles is very short, approximately 6.5 ms. Using the 0% command level, this corresponds to approximately 20 deg of roll at this roll rate.

Body-fitted mixed-element-type unstructured grids were generated that were suitable for both inviscid and viscous simulations. The volume grids were constructed using the advancing-front/local-reconnection (AFLR) grid-generation technique.[4] SolidMesh was used to prepare the CAD geometry and generate surface grids.[5] An emphasis was placed on capturing the vortices generated by the canards and resolving them along the missile body to ultimately determine if they impinge on the tail fins. To help control the field resolution near the canard tips, an embedded surface was constructed around the missile to better control the point spacing and the growth of the cell sizes in this region. This allowed fine resolution for the field grid between this surface and the missile and coarse resolution for the field grid between this surface and the far field. The embedded surface surrounding the missile was approximately 3 diameters (of the missile body) in width in order to encapsulate the vortices generated by the canards.

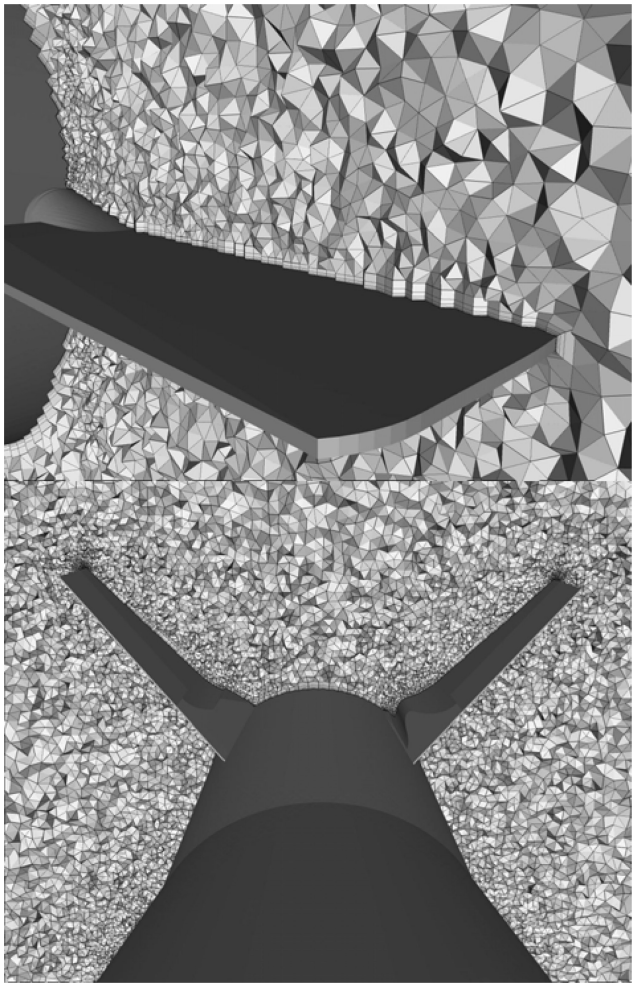

Fig. 3 Cutting planes through the unstructured mesh.

A grid-resolution study, the results of which are discussed later, was conducted to provide insight into the impact of the grid spacing on the aerodynamic performance prediction for the spinning missile. Three grids, referred to as coarse, medium, and fine, were generated for both the inviscid and viscous cases. The surface grids for the inviscid and the corresponding viscous grids are essentially the same. However, the inviscid surface grids required additional resolution near corner regions to resolve expansions. The total number of grid points in the coarse, medium, and fine inviscid grids was 3.06×10^6, 3.34×10^6, and 4.74×10^6, respectively. The coarse, medium, and fine viscous volume grids contained 7.29×10^6, 7.89×10^6, and 9.26×10^6 grid points, respectively. For the viscous grids, the normal spacing of the first grid point from the body was 1.0×10^{-5}, which lead to a $y+$ distribution of less than 1.0 over the missile, thus indicating good viscous sublayer resolution. Cutting planes taken through field of the medium-resolution viscous grid are shown in Fig. 3 to illustrate the boundary-layer and field resolution. Aside from the boundary-layer resolution, the field resolution is similar between the corresponding inviscid and viscous grids.

Solution Technique

Governing Equations

The unsteady three-dimensional compressible Reynolds-averaged Navier–Stokes equations are presented here in Cartesian coordinates and in conservative form. The nondimensional equations can be written in integral form as follows:

$$\frac{\partial}{\partial t}\int_{\Omega} \boldsymbol{Q}\,\mathrm{d}V + \int_{\partial\Omega} \boldsymbol{F}\cdot\hat{\boldsymbol{n}}\,\mathrm{d}A = \frac{M_\infty}{Re}\int_{\partial\Omega} \boldsymbol{G}\cdot\hat{\boldsymbol{n}}\,\mathrm{d}A \qquad (1)$$

The vector of dependent variables and the components of the inviscid and viscous fluxes are

$$\boldsymbol{Q} = \begin{bmatrix} \rho \\ \rho u \\ \rho v \\ \rho w \\ E \end{bmatrix}, \qquad \boldsymbol{F}\cdot\hat{\boldsymbol{n}} = \begin{bmatrix} \rho\Theta \\ \rho u\Theta + \hat{\boldsymbol{n}}_x P \\ \rho v\Theta + \hat{\boldsymbol{n}}_y P \\ \rho w\Theta + \hat{\boldsymbol{n}}_z P \\ \rho H\Theta - a_t P \end{bmatrix}$$

$$\boldsymbol{G}\cdot\hat{\boldsymbol{n}} = \begin{bmatrix} 0 \\ \hat{\boldsymbol{n}}_x\tau_{xx} + \hat{\boldsymbol{n}}_y\tau_{xy} + \hat{\boldsymbol{n}}_z\tau_{xz} \\ \hat{\boldsymbol{n}}_x\tau_{yx} + \hat{\boldsymbol{n}}_y\tau_{yy} + \hat{\boldsymbol{n}}_z\tau_{yz} \\ \hat{\boldsymbol{n}}_x\tau_{zx} + \hat{\boldsymbol{n}}_y\tau_{zy} + \hat{\boldsymbol{n}}_z\tau_{zz} \\ \boldsymbol{u}\cdot(\tau\cdot\hat{\boldsymbol{n}}) - \boldsymbol{q}\cdot\hat{n} \end{bmatrix} \tag{2}$$

The velocity normal to a control volume face is defined as

$$\Theta = \hat{\boldsymbol{n}}_x u + \hat{\boldsymbol{n}}_y v + \hat{\boldsymbol{n}}_z w + a_t \tag{3}$$

and the grid speed is defined as

$$a_t = -(V_x\hat{\boldsymbol{n}}_x + V_y\hat{\boldsymbol{n}}_y + V_z\hat{\boldsymbol{n}}_z) \tag{4}$$

Note that $\boldsymbol{V}_s = V_x\hat{\boldsymbol{i}} + V_y\hat{\boldsymbol{j}} + V_z\hat{\boldsymbol{k}}$ is the control volume face velocity. The variables in the preceding equations are nondimensionalized using a characteristic length and freestream values of velocity, speed of sound, density, and viscosity. Thus, the Reynolds number is defined as $U_\infty L/\nu_\infty$ and the Mach number is defined as U_∞/a_∞. Pressure is normalized by $P^*/\rho_\infty a_\infty^2$, where P^* is the local dimensional static pressure. The viscous stresses are

$$\tau_{ij} = (\mu + \mu_t)\left(\frac{\partial u_i}{\partial x_j} + \frac{\partial u_j}{\partial x_i}\right)$$

The system of equations is closed by using the equation of state for a perfect gas:

$$P = \rho RT \tag{5}$$

Solution Algorithm Details

The simulations were performed using the U^{2}NCLE unstructured flow solver.[6] U^{2}NCLE is a parallel flow simulation code that solves the unsteady Reynolds-averaged Navier–Stokes equations for complex geometries represented by multi-element unstructured grids. U^{2}NCLE is capable of solving inviscid, laminar, and high-Reynolds-number flows for either steady or unsteady conditions. An overview of the U^{2}NCLE solution algorithm is presented here.

The U^{2}NCLE flow solver is a node-centered, finite volume, implicit scheme applied to general unstructured grids with nonsimplical elements. The flow variables are stored at the vertices and surface integrals are evaluated on the median dual surrounding each of these vertices. The nonoverlapping control volumes formed by the median dual completely cover the domain and form a mesh that is dual to the elemental grid. Thus, a one-to-one mapping exists between the edges of the original grid and the faces of the control volumes.

The solution algorithm consists of the following basic steps: reconstruction of the solution states at the control volume faces, evaluation of the flux integrals for each control volume, and the evolution of the solution in each control volume in time. The inviscid fluxes are computed using Roe's flux-difference splitting technique.[7] A second-order (in space) method is used for the inviscid flux terms and Barth's limiter is also applied to these terms. The temporal discretization is done using a second-order in time backward Euler implicit scheme. The time evolution is accomplished using a Newton relaxation scheme to advance the unsteady solution at each time step.[8] The one-equation turbulence model by Spalart and Allmaras was used for simulation of turbulent effects in high-Reynolds-number flows.[9]

For efficiency, it is essential to parallelize the flow solution algorithm. The present parallel unstructured viscous flow solver is based on coarse-grained domain decomposition for concurrent solution within subdomains assigned to multiple processors. The solution algorithm employs iterative solution of the implicit approximation with the iteration hierarchy as shown in Fig. 4. In addition, domain decomposition takes place with each subdomain uniquely mapped to a given processor. The code employs the Message Passing Interface standard for interprocessor communication.

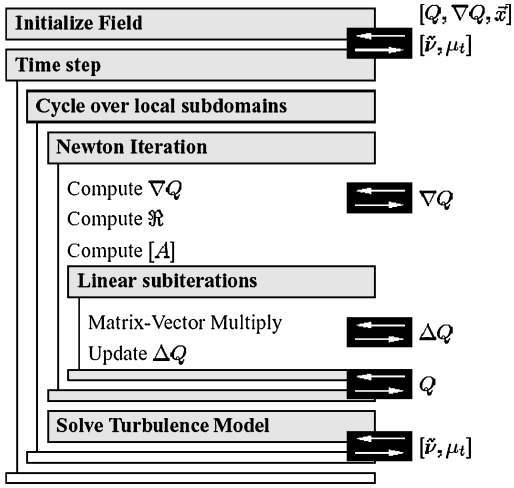

Fig. 4 U^{2}NCLE flow solver iteration hierarchy.

The relative motion of the canard dithering was simulated using a local grid-reconnection technique. The canard surface grid and a small region of the surrounding volume grid are rigidly rotated each time step as prescribed by the canard deflection of the command level. The volume grid is then locally reconnected in this region.

Simulation Results

Unsteady Euler and Navier–Stokes simulations were performed to predict the flowfield and force and moment coefficients for the spinning missile. These simulations were used to provide insight into the impact of viscous effects and grid resolution on the prediction of the spinning missile's aerodynamic performance. All of the simulations performed used the following parameters: $M = 1.6$, $\alpha = 3$ deg, $\Omega = 8.75$ Hz. At these conditions, a particle travels approximately 36.6 body lengths in one revolution. The viscous simulations were conducted using a Reynolds number of $Re = 41.3 \times 10^6$. Unless stated otherwise, the results presented here were obtained using the fine viscous grid.

The force coefficients are defined using the standard normalization by dynamic pressure:

$$C_F = \frac{\text{Force}}{\frac{1}{2}\rho_\infty U_\infty^2 S} \tag{6}$$

Similarly, the moment coefficients are

$$C_M = \frac{\text{Moment}}{\frac{1}{2}\rho_\infty U_\infty^2 SL} \tag{7}$$

where the reference area S is the cross-sectional area of the missile body and the reference length L is the length of the missile. The moments were computed about the missile center of gravity.

The flowfield about this missile is characterized by complex vortical flow and shock structures. The canards are thin supersonic airfoils with sharp edges that generate shocks and expansions. The canards also generate strong horseshoe vortices that convect the length of the missile. The horseshoe vortex is generated due to the decrease in lift at the canard tips. Because the missile is spinning, the vortices tend to twist around the missile. At this low angle of attack, the vortices are also close enough to the missile body to affect the force distribution on the fuselage and tail. A detached bow shock

is formed ahead of the blunt, hemispherical-shaped nose and intersecting shocks and expansion are formed around the canards and tail fins.

Helicity was used to detect or track the vortices generated by the canards. Helicity is a measure of the helical motion of the fluid and is defined as follows:

$$H = \boldsymbol{V} \cdot (\boldsymbol{\nabla} \times \boldsymbol{V}) = \boldsymbol{V} \cdot \boldsymbol{\omega} \tag{8}$$

Because of the magnitude of H, $\pm \log_{10}(|H|)$ is actually plotted and $\pm$ was used depending on the original sign of H. Note that values of H in the range $-1 \leq H \leq 1$ were set to zero. The planes on which helicity is plotted are located at $x/L = 0.15$, 0.2, 0.3, 0.4, 0.5, 0.6, 0.7, 0.8, and 0.9.

Solver Convergence Studies

Preliminary CFD simulations were performed to determine the proper solver parameters to ensure that the unsteady solution was converged at each time step. The convergence studies were performed with the coarse viscous grid. The U^{2}NCLE flow solver uses Newton's method for the time evolution. Newton's method linearizes the equations about a given time level and results in a linear system of equations that must be solved. This linear system of equations is solved using a symmetric Gauss–Seidel scheme. Multiple Newton iterations are used to rid the solution of time linearization error at a given time step. Multiple linear subiterations are performed to solve the system of equations arising from the implicit discretization of the governing equations. For the results presented here, eight linear subiterations were used.

Time-step studies were done using Δt corresponding to 0.5, 1.0, and 2.0 deg of roll per time step. There was very little difference between the force and moment coefficient results between 0.5 and 1.0 deg per time step. Using $\Delta t = 2$ deg per step did not provide adequate resolution in the canard transition regions and tended to "clip" the results. Thus, it was decided to use the time-step value of $\Delta t = 1.0$ deg per time step for all the simulations. In all cases, the solution was found to be periodic within one revolution.

Convergence studies were also performed to determine the number of Newton iterations needed per time step. Three, four, and five Newton iterations were used. Except for the axial force, the results were the same when using four and five Newton iterations. The axial force was converged via the fourth Newton iteration; hence, four Newton iterations were used for the results presented here.

Grid-Resolution Study

A localized grid-resolution study was performed. Additional grid points were added in regions of interest to help resolve salient flow features. Because the canard vortices are suspected of impinging on the tail fins and these vortices have an impact on the force and moment distribution acting on the missile, their resolution was important and was used as a guide in determining regions to add points to the grid.

In the coarse inviscid grid, the root vortices are dissipated completely by $x/L = 0.5$. Note that in an inviscid solution there is no physical mechanism (i.e., viscous dissipation) to generate the vortices and they are caused by the numerical dissipation in the flux-computation scheme. And because there is no physical dissipation, once they are created, numerical dissipation of one form or another is responsible for their disappearance. The root vortices are lost due to the dissipation inherent in the solution method. The dissipation is highly dependent on the grid resolution. The location $x/L = 0.5$ is where the maximum aspect ratio of the surface grid occurs along the missile body. This stretching in turn causes larger-volume cells to be generated, which tend to dissipate the vortices. The tip vortex was not dissipated nearly as soon and can be detected up to $x/L = 0.8$. In the viscous solution, both vortices are weakly resolved to the end of the missile.

Because of the dissipation introduced by the grid resolution on the vortices, the maximum aspect ratio in the fuselage surface grid was reduced from 5:1 to 2:1 for the medium refinement grids. For the inviscid solution, this refinement increased the resolution of the root vortex, but it still is dissipated by $x/L = 0.7$. The tip vortex was resolved to the end of the missile. For the viscous solution, the refinement improved the resolution and strength of the root vortex and both vortices were resolved to the end of the missile. For the fine grids, nearly 1.5 million points were added to the field of both the inviscid and viscous grids. The additional refinement increased the resolution of the root vortex for the inviscid solution, but it is still dissipated before the end of the missile. Thus, more refinement is necessary for the inviscid solution to represent the root vortex. A comparison of the helicity contours taken from the fine inviscid and viscous grids is shown in Fig. 5.

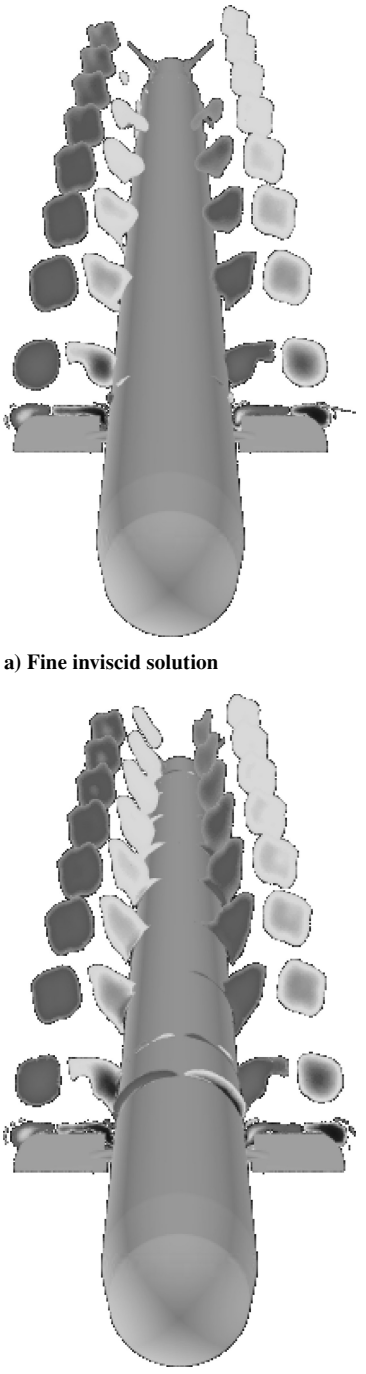

a) Fine inviscid solution

b) Fine viscous grid solution

Fig. 5 Log_{10} helicity contours at $\theta = 0$ deg.

A summary of the roll-averaged (i.e., the average value over a single revolution) force and moments is listed in Table 1 for the inviscid and viscous grids. For both the inviscid and viscous grids, the axial force was affected most by the grid refinements. The change in axial force is likely due to the additional resolution of the canard

Table 1 Roll-averaged force and moment coefficients for the grid-resolution study

Solution	Grid	C_A	C_Y	C_N	C_l	C_m	C_n
Inviscid	Coarse	1.1455	7.538$e-4$	0.4823	−5.908$e-4$	−1.812$e-3$	6.602$e-4$
Inviscid	Medium	1.1452	2.692$e-3$	0.4682	−6.492$e-4$	−3.686$e-3$	1.111$e-3$
Inviscid	Fine	1.1397	−1.187$e-3$	0.4674	−7.304$e-4$	−4.484$e-3$	1.282$e-3$
Viscous	Coarse	1.193	2.651$e-3$	0.4803	−5.704$e-4$	1.230$e-4$	2.263$e-4$
Viscous	Medium	1.178	4.464$e-3$	0.4677	−5.668$e-4$	−1.319$e-3$	7.096$e-4$
Viscous	Fine	1.179	−2.391$e-4$	0.4694	−5.791$e-4$	−2.569$e-3$	3.387$e-4$

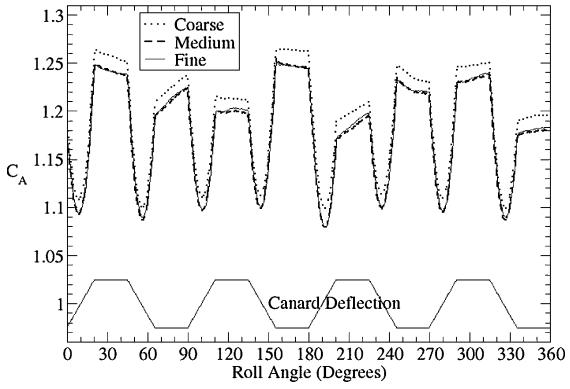

a) Axial force coefficient

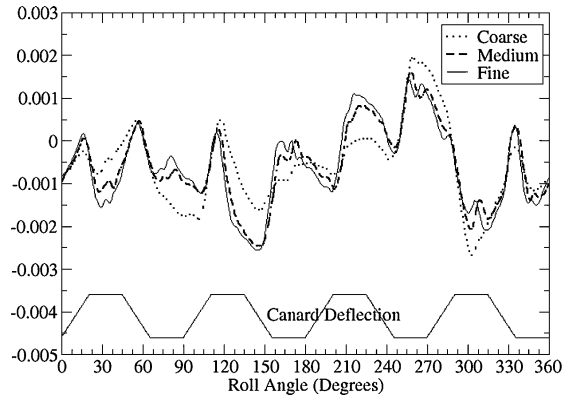

b) Rolling moment coefficient

Fig. 6 Viscous grid-refinement study.

root vortices farther aft along the body. The side and normal force coefficients are almost identical among all three grids. The rolling moment coefficient also varied as the grids were refined. The pitching and yawing moments show differences between the coarse- and medium-refinement grids, but little change between the medium- and fine-resolution grids. The axial force and rolling moment coefficient histories for the viscous grid convergence simulations are shown in Fig. 6. Aside from the axial force and rolling moment, the viscous medium-refinement grid appears to be sufficient to predict the forces and moments acting on the missile. As mentioned previously, the inviscid grid needs further refinement to represent the root vortex to the end of the missile.

Viscous vs Inviscid Solution Comparison

The dynamic forces acting on a missile can be broken down into inertial (pressure) and viscous (shear) components. Typically, for low angles of attack, the flow is not separated and inertial forces dominate. For such cases, good agreement with experimental data can be achieved using potential flow or Euler codes. For moderate and higher angles of attack, the flow is turbulent and is characterized by large-scale boundary-layer separation. Consequently, the viscous effects are important, and it becomes essential to use a Navier–Stokes code to correctly model the physics of the flow.

Inviscid and viscous simulations were conducted to provide insight into the impact of the viscous effects on the aerodynamic performance of the spinning missile. Figure 7 compares the viscous and inviscid force and moment coefficients. The viscous axial force is larger by a nearly constant amount than the inviscid axial force, which is to be expected because the inviscid solution neglects the shear stress due to skin friction along the body. Note, however, that the difference between the inviscid and viscous axial force should be slightly larger, except that the inviscid solution overexpands the flow at the aft end of the missile, which lowers the base pressure and consequently increases the axial force. Compared to the viscous solution, the inviscid solution results tend to overpredict the side and normal forces when the canards are at their maximum deflection. The differences in the side force are most noticeable when the missile is in the 90- and 270-deg orientations, that is, when side force is the largest. The magnitude of the inviscid root vortex is slightly larger than the viscous one and, thus, provides a larger pressure differential across the canard, which in turn generates more side force. Similarly for the normal force, the largest differences occur when the normal force is the largest, in the 0- and 180-deg orientations. The slightly larger inviscid root vortex provides a larger pressure differential between the upper and lower surfaces of the canard and generates additional normal force. These same trends are observed in the pitching and yawing moments because the normal force generates the pitching moment and the side force the yawing moment.

During the times when the canards transition between their minimum and maximum deflection, there is virtually no difference between the inviscid and viscous forces and moments. Aside from the axial force, there is very little overall difference between the two solutions. This is not surprising because the flow is supersonic and pressure forces tend to dominate. In addition, the angle of attack is low and so the flow remains attached and, thus, there are no regions in the flow where viscous effects are significant. Figure 8 shows the viscous force contributions. The viscous effects (i.e., shear stress contributions) contribute approximately 8–10% of the total axial force and the remaining portion of the force is due to normal stress (pressure) contributions. For the normal force, the viscous forces are only responsible for 2–3% of the total force except at the $\theta =$ 0- and 180-deg orientations when the normal force is a maximum. The viscous effects for the side force are negligible except at locations where the canard transitions from ± 15 deg.

To provide additional insight, the forces from the fine viscous grid solution were decomposed by component as shown in Fig. 9. As expected, the fuselage was responsible for the majority of the axial force because it has the largest wetted surface area of any of the components. For the canard component, the plateau regions correspond to when the canard is at maximum deflection and, thus, has a maximum surface area exposed to the flow. Note that the axial force acting on the base region is acting in the opposite direction of the other forces. The forces acting on this surface are strictly pressure forces, which are due to the pressure drag caused by the expansion at the end of the missile. Because of the orientation and symmetry of this surface, the forces acting on this surface are only in the axial direction and have no contribution to the side or normal forces or any of the moments.

The canards generate nearly all of the side force and consequently are responsible for nearly all of the yawing moment. Even though the fuselage is axisymmetric, it generates some side force because it is spinning due to the Magnus effect. The variation of the fuselage side force is in phase with that of the canards, indicating the strong vortices shed from the canards are modifying the pressure distribution along the fuselage. The tail generates almost no side force due to its symmetry, but the small amount of side force generated by the tail is out of phase or opposite to that generated by the canards. This

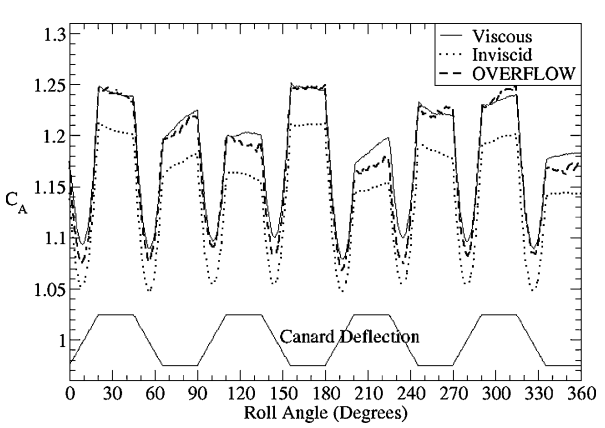

a) Axial force coefficient

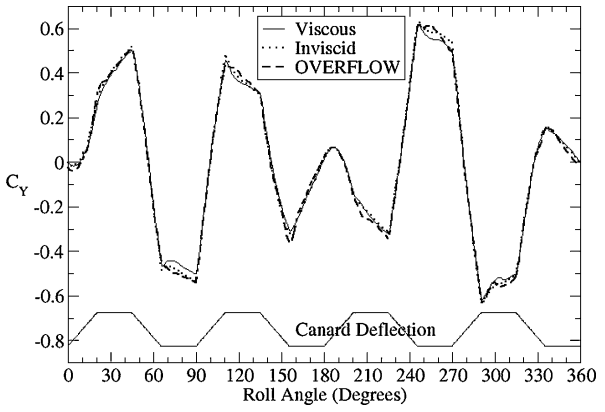

b) Side force coefficient

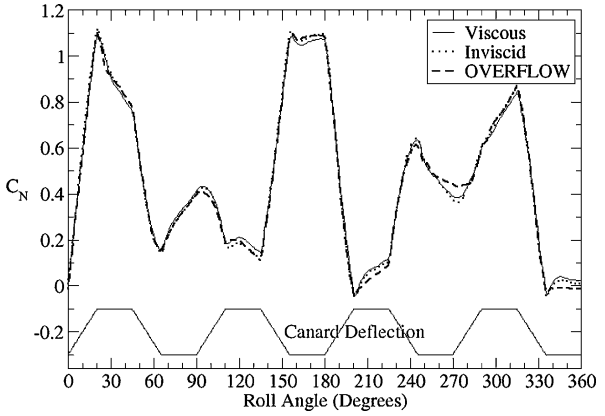

c) Normal force coefficient

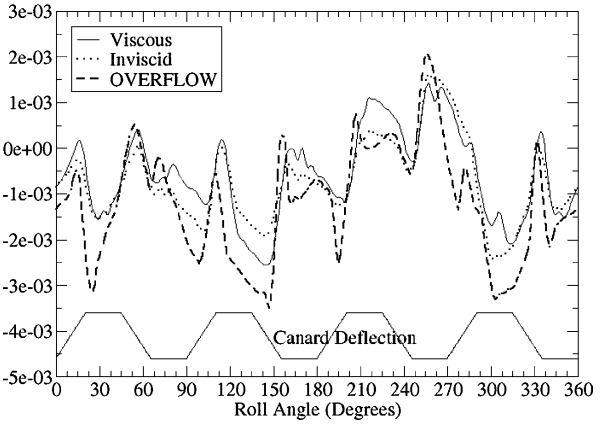

d) Rolling moment coefficient

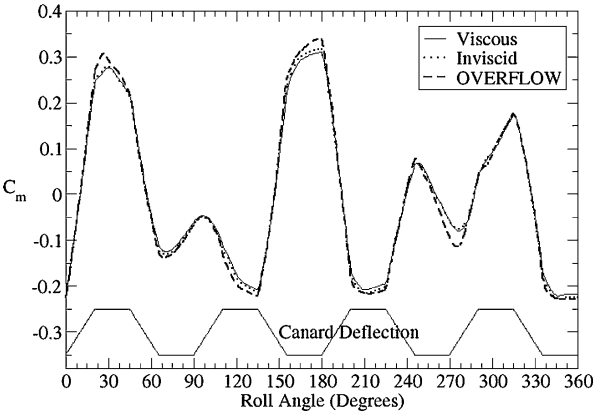

e) Pitching moment coefficient

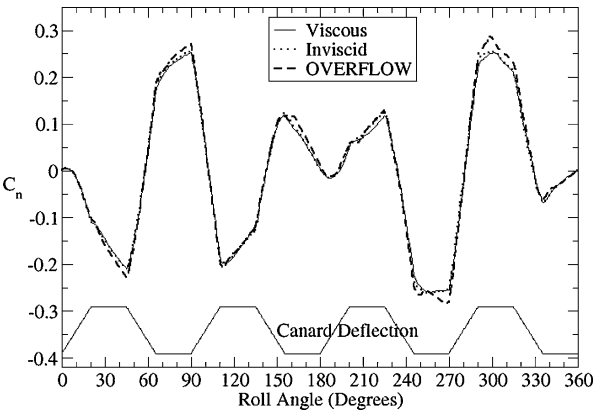

f) Yawing moment coefficient

Fig. 7 Viscous vs inviscid solution comparison.

variation in the tail force indicates that the vortices generated by the canards travel the length of the body and are still strong enough to modify the pressure distribution on the tail. The tail force is out of phase with the canards because the canards are in their maximum or minimum deflection for approximately 20 deg, but it takes nearly 10 deg of roll for a particle to travel from the canards to the tail.

All of the components have significant normal force contributions. As in the case of the side force, the tail component is out of phase with the canard normal force. Near the maximum canard lift orientations, $\theta = 0$ and 180 deg, the fuselage and tail also generate their maximum normal force contributions, indicating that the vortices shed from the canards modify the pressure distribution on the fuselage and tail to increase the normal force. The canards also generate the majority of the pitching moment with some contribution from the tail.

To determine whether the canard vortices impinge on the tail, helicity field contours were generated every time step. Upon inspection, it was discovered that, for these conditions and 0% command level, the vortices do impinge on the tail fins at two roll orientations, $\theta = 90$ and 270 deg, as indicated in Fig. 10. At this orientation, some twist in the vortices is evident.

Simulations were also made using the 100% canard command level. The force and moment coefficient histories are shown in Fig. 11. The variation in the loading coincides with the canard movement, just as in the solution using the 0% canard command level. A comparison of the roll-averaged force and moments is listed in Table 2. For both the 0 and 100% command levels, the area under the canard deflection curve is zero and thus should not induce any net lateral motion of the missile over one revolution. Inspection of Table 2 reveals that the side force and yawing coefficients are zero or nearly zero, indicating no lateral movement. The 100% command level had a significantly larger normal force coefficient and, consequently, larger pitching moment coefficient, because the canards remain in their maximum deflection positions longer compared to

Table 2 Roll-averaged force and moment coefficients for the 0 and 100% command levels

Solution	Command level, %	C_A	C_Y	C_N	C_l	C_m	C_n
Inviscid	0	1.1397	−1.187e−3	0.4674	−7.304e−4	−4.484e−3	1.282e−3
Inviscid	100	1.1669	0.04821	0.6936	−6.436e−4	0.1184	−0.01997
Viscous	0	1.1794	−0.0002	0.4694	−0.0006	−0.0026	0.0003
Viscous	100	1.1996	0.04817	0.6875	−5.769e−4	0.1157	−0.01958

Table 3 Roll-averaged force and moment coefficients for the viscous solver comparison

Solution	C_A	C_Y	C_N	C_l	C_m	C_n
OVERFLOW-D[3]	1.172	−7.56e−3	0.461	−1.19e−3	−6.79e−3	2.80e−3
U^{2}NCLE	1.179	−2.39e−4	0.469	−5.79e−4	−2.57e−3	3.39e−4

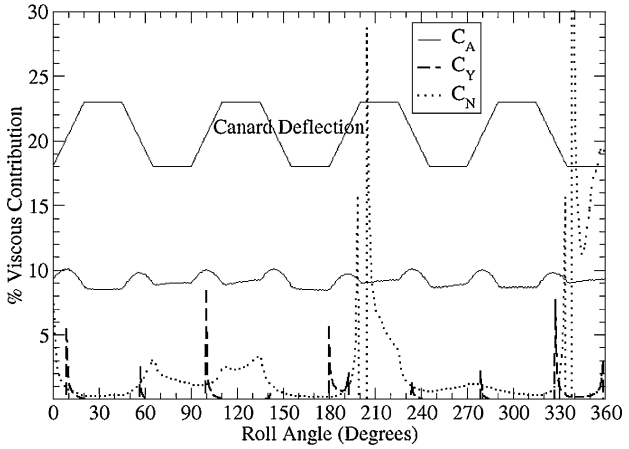

Fig. 8 Percentage of viscous force contribution to the total force.

the 0% command level. This also resulted in the 100% command level having a slight increase in the axial force coefficient because the maximum frontal area of the canards is exposed for a longer period of time.

Computational and Experimental Comparison

The results generated using U^{2}NCLE were compared to the results generated using the OVERFLOW-D flow solver.[3] While both codes are high-resolution Navier–Stokes flow solvers, OVERFLOW-D represents a different approach to solving this type of complex problem involving relative grid motion. Whereas U^{2}NCLE uses an unstructured-grid methodology, OVERFLOW-D uses a Chimera overset structured-grid methodology. The OVERFLOW-D results were generated using an extremely fine spatial and temporal resolution: 41 million grid points and 12,000 time steps per revolution. A comparison of the force and moment coefficients for the viscous solution to those generated using the OVERFLOW-D code is shown in Fig. 7 and the roll-averaged values are compared in Table 3. The roll-averaged results agree very well and, qualitatively, the force and moment coefficient roll histories compare well with the most noticeable difference occurring at roll angles of 120 and 210 deg. The differences are likely due to the increase in resolution of the OVERFLOW-D grid, 41 million vs 9 million points. However, it is difficult to draw any definitive conclusion other than that both methodologies predict nearly similar results and the lack of significant differences indicates that both codes offer viable approaches to solving this class of problem.

In an attempt to verify the accuracy of the results predicted by the solver, a comparison was made with experimental data.[10] A simulation was performed representative of one of the experimental tests, which included the ability to simultaneously roll the missile and to dither the canards. The actual motion of the canards during the experiment was averaged over 10 body revolutions and an analytical approximation to the ensemble average was used to dither the canards in the simulation.[1] The curve labeled Exp-Fit in Fig. 2 represents the analytic approximation that was used in the simulation and this command level is also periodic over one body revolution.

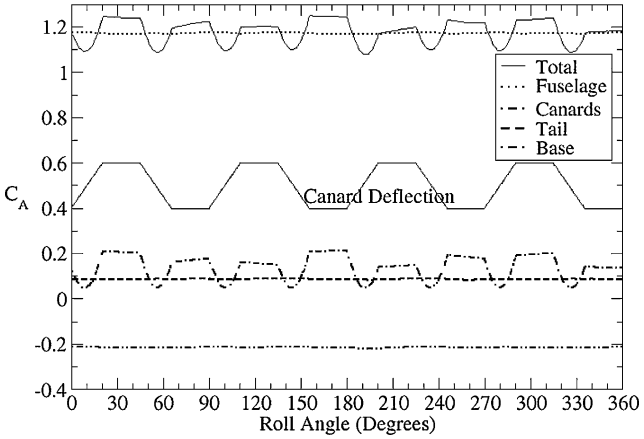

a) Axial force coefficient

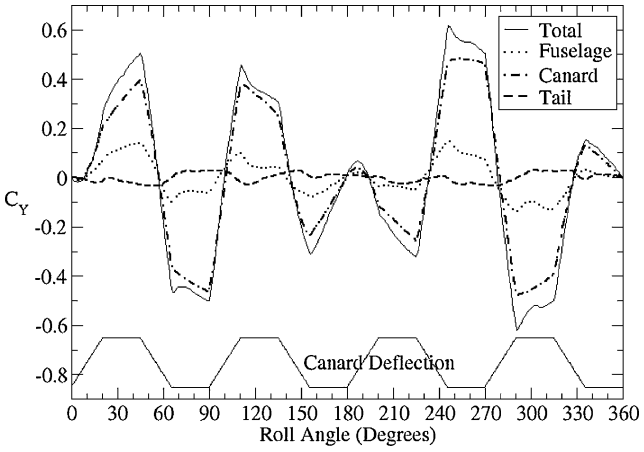

b) Side force coefficient

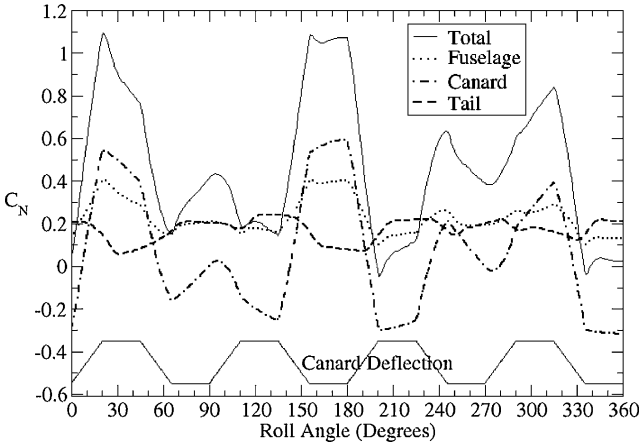

c) Normal force coefficient

Fig. 9 Viscous solution component contributions.

Table 4 Roll-averaged force and moment coefficients for the experimental command level

Solution	C_A	C_Y	C_N	C_l	C_m	C_n
Experiment[10]	1.155–1.176	0.15–0.20	0.45–0.61	−0.036–−0.019	−1.5–−0.39	0.93–1.5
U^{2}NCLE	1.155	0.22	0.51	−0.023	−0.77	1.5

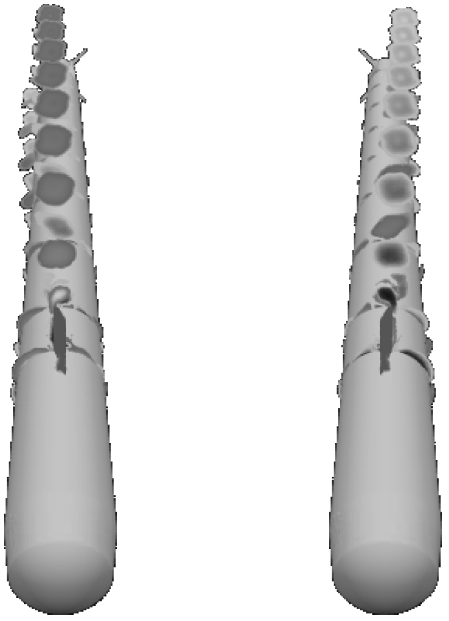

a) $\theta = 90$ deg **b) $\theta = 270$ deg**

Fig. 10 Helicity contours for 0% canard command level.

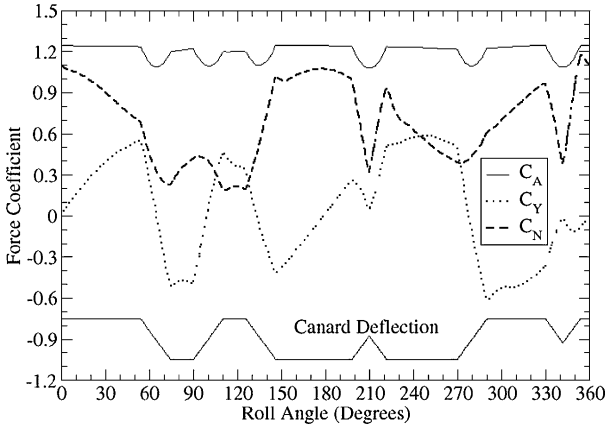

a) Force coefficients

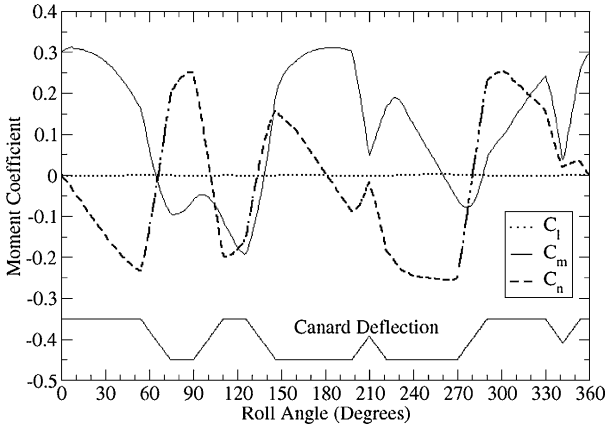

b) Moment coefficients

Fig. 11 Loading history using the 100% canard command level.

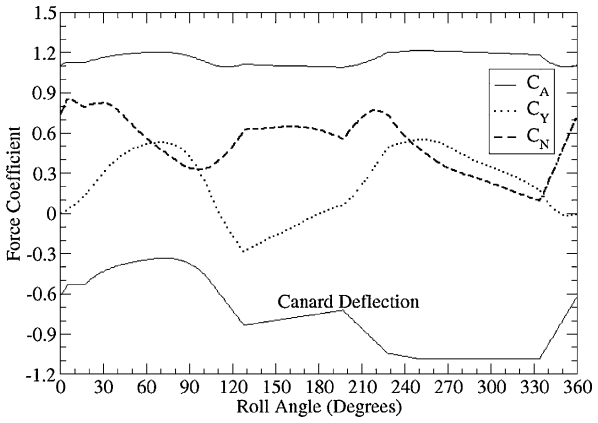

a) Force coefficients

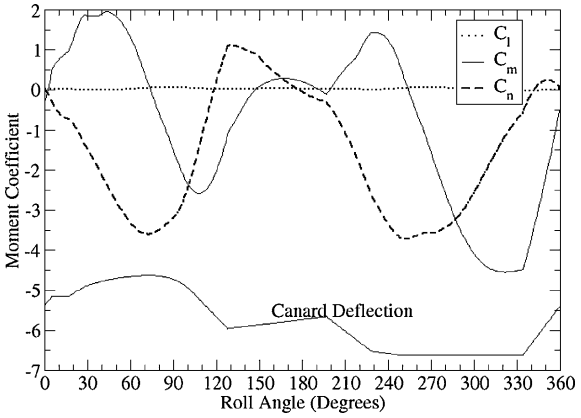

b) Moment coefficients

Fig. 12 Loading history using the experimental canard command level.

The run conditions were $M = 1.6$, $\alpha = 3.0$ deg, and $\Omega = 18.0$ Hz. The computed force and moment coefficients are shown in Fig. 12. As before, the influence of the canard motion is quite evident. This command level produces a starboard yaw movement of the missile, whereas the 0 and 100% command levels resulted in zero or very small side forces. The roll-averaged forces are compared against the experimental values in Table 4. Note that the experimental axial force coefficient includes the contribution from the base region but not the correction for buoyancy, which is an experimentally derived quantity accounting for the nonzero pressure gradient in the streamwise direction of the wind tunnel.[10] Except for the side force coefficient, the results are within the bounds of the experimental uncertainty. Over the 10 body revolutions, the experimental dither pattern has significant variation (approximately 7 deg) in the canard deflection angle around $\theta = 160$ to 180 deg and deviates significantly from the curve fit. This could potentially affect the side force coefficient, but further investigation is required. Overall, the results compare very well.

Computational Expense

All simulations were performed on a 1038 processor Linux cluster having 1-GHz processors each with 512 MB of RAM. A single time step for the fine inviscid grid took on average 320 s (32 h per revolution) utilizing 32 processors with approximately 150,000 points per processor. The fine viscous grid took 36.5 h to obtain a solution for a single revolution (365 s per time step) utilizing 70 processors with approximately 133,000 points per processor. A

steady-state case was also run using the fine viscous grid. Utilizing the same number of processors as before, each time step or iteration took on average 71 s. For the steady case, only a single Newton iteration was performed each time step and there was no relative grid motion and, consequently, less time was required per iteration.

Summary

Viscous and inviscid solutions were obtained to predict the aerodynamic performance of a spinning missile with dithering canards. An unstructured-grid approach was successfully demonstrated to simulate the relative motion of the canards. Force and moment coefficients were computed along with helicity contours to track the vortices being generated by the canards. Comparisons were made to determine the effect of grid resolution and viscous effects on prediction of aerodynamic performance.

The grid resolution indicated that the force and moment coefficients generated using the medium-refinement grid were in agreement with those using the fine grid. Comparison of the viscous and inviscid force and moment coefficients revealed that the viscous effects were not significant for this case. The largest viscous contribution was to the axial force, which was approximately 10% of the total axial force. Overall, the viscous effects were minimal because the flow is supersonic and at this low angle of attack the flow remains attached and there are no regions of separated flow where viscous effects are important. Thus, depending on the solution requirements, the inviscid solution may be used to predict the aerodynamic performance of the missile with good accuracy. Examining the helicity contours, it was found that vortices do impinge on the tail fins at two roll orientations, $\theta = 90$ and 270 deg. Comparisons of the viscous solution were made with results from another high-resolution viscous flow solver and with experimental data and the results compared favorably with both.

Acknowledgments

The authors thank Tor Nygaard of Eloret and Robert Meakin of the U.S. Army Aeroflightdynamics Directorate at NASA Ames Research Center for providing the OVERFLOW-D simulation results for comparison. The authors also thank Scott Murman of Eloret and Michael Aftosmis of NASA Ames Research Center for providing the canard command schedule used for the comparison with the experimental data.

References

[1]Murman, S. M., Aftosmis, M. J., and Berger, M. J., "Numerical Simulation of Rolling Airframes Using a Multilevel Cartesian Method," *Journal of Spacecraft and Rockets* (to be published).

[2]Hall, L. H., "Chimera Moving Body Methodology for Rolling Airframe Missile Simulation with Dithering Canards," AIAA Paper 2002-2801, June 2002.

[3]Nygaard, T. A., and Meakin, R. L., "Aerodynamic Analysis of a Spinning Missile with Dithering Canards," *Journal of Spacecraft and Rockets* (to be published); also AIAA Paper 2002-2799, June 2002.

[4]Marcum, D. L., "Efficient Generation of High Quality Unstructured Surface and Volume Grids," *Engineering with Computers*, Vol. 17, No. 3, 2001, pp. 211–233.

[5]Gaither, J. A., Marcum, D. L., and Mitchell, B., "SolidMesh: A Solid Modeling Approach to Unstructured Grid Generation," *7th International Conference on Numerical Grid Generation in Computational Field Simulations*, edited by B. K. Soni, J. Haeuser, J. F. Thompson, and P. R. Eiseman, International Society of Grid Generation, Mississippi State, MS, 2000, pp. 829–838.

[6]Hyams, D. G., Sreenivas, K., Sheng, C., Briley, W. R., Marcum, D. L., and Whitfield, D. L., "An Investigation of Parallel Implicit Solution Algorithms for Incompressible Flows on Multielement Unstructured Topologies," AIAA Paper 2000-0271, Jan. 2000.

[7]Roe, P., "Approximate Riemann Solvers, Parameter Vectors, and Difference Schemes," *Journal of Computational Physics*, Vol. 43, No. 2, 1981, pp. 357–372.

[8]Whitfield, D. L., and Taylor, L., "Discretized Newton-Relaxation Solution of High Resolution Flux-Difference Split Schemes," AIAA Paper 91-1529, June 1991.

[9]Spalart, P. R., and Allmaras, S. R., "A One-Equation Turbulence Model for Aerodynamic Flows," *La Recherche Aerospatiale*, No. 1, 1994, pp. 5–21.

[10]"Defensive Missile Wind Tunnel Test for the Validation and Verification of CFD Codes," Dynetics, Technical Rept., Huntsville, AL, Jan. 2002.

R. M. Cummings
Associate Editor